Research Square

Preprints are preliminary reports that have not undergone peer review.
They should not be considered conclusive, used to inform clinical practice,
or referenced by the media as validated information.

HDAC10 preserves genome stability by regulating PCM1 and p53 through chaperone-mediated autophagy

Joo-Yong Lee

leejooyong@cnu.ac.kr

Chungnam National University https://orcid.org/0000-0003-1049-6006

Kim Uigeun

Sovannarith Korm

Harvard Medical School https://orcid.org/0000-0003-2211-2946

Myung Hun Kim

Chungnam National University

Dong-Uk Kim

Chungnam National University

Minh Hieu Vu

Chungnam National University

Jihye Kim

Chungnam National University

Article

Keywords: HDAC10, chaperone mediated autophagy (CMA), genomic instability, PCM1, p53, senescence

Posted Date: November 10th, 2026

DOI: https://doi.org/10.21203/rs.3.rs-11246803/v1

License: This work is licensed under a Creative Commons Attribution 4.0 International License.
Read Full License

Additional Declarations: (Not answered)

Abstract

Genomic instability promotes malignant evolution in cancer, whereas DNA-damage-induced senescence acts as a barrier to the propagation of cells with chromosome abnormalities. Disruption of these protective responses permits the persistence and selection of genetically abnormal clones. Here, we show that HDAC10 deficiency induces chaperone-mediated autophagy dependent degradation of PCM1 and p53, compromising chromosome stability and senescence-associated growth restraint, respectively. Supporting clinical relevance, breast cancer datasets associated higher HDAC10 expression with favorable patient survival, revealed an inverse correlation between HDAC10 and LAMP2 expression, and showed a reciprocal pattern of higher HDAC10 and lower LAMP2 expression in patients responding to DNA damaging anthracycline chemotherapy. Our findings identify HDAC10 as a regulator linking CMA-dependent proteostasis to genome stability and cellular senescence. By preserving PCM1 and p53, HDAC10 supports mitotic fidelity and p53-dependent senescence, thereby limiting chromosome instability and the persistence of genomically unstable cells. Disruption of this regulatory axis therefore provides a mechanism by which chromosome instability and impaired senescence cooperate during malignant progression in breast cancer.

Introduction

Maintenance of genome stability requires coordinated control of chromosome segregation, DNA repair, and senescence [1, 2]. Disruption of these processes can generate chromosome-number abnormalities and micronuclei, thereby promoting further genomic instability [3, 4]. The persistence of genomic instability activates checkpoint pathways that influence whether cells repair the damage, undergo sustained growth arrest, or are eliminated [5]. The tumor suppressor p53 is a central regulator of these decisions and contributes to senescence in response to genotoxic stress [6, 7, 8]. Thus, coordination between chromosome-maintenance mechanisms and p53-dependent senescence is essential for preventing the persistence and propagation of genomically unstable cells.

Chaperone-mediated autophagy (CMA) is a selective lysosomal pathway in which heat shock cognate 70 (HSC70) recognizes soluble substrates containing KFERQ-like targeting motifs [9]. These substrates are delivered to lysosome-associated membrane protein type 2A (LAMP2A), unfolded, and translocated across the lysosomal membrane for degradation [9]. Accumulating evidence suggests a connection between CMA and genome maintenance [10, 11]. CMA regulates the turnover of the checkpoint kinase CHK1 following DNA damage, demonstrating that selective lysosomal degradation participates in the control of DNA-damage responses [10]. CMA also contributes to the homeostasis of pericentriolar material 1 (PCM1), through a DNAJA2–HSC70-dependent mechanism [11]. PCM1 is a major centriolar satellite scaffold that supports centrosomal protein recruitment and microtubule organization [12, 13], suggesting that dysregulated PCM1 turnover could compromise processes required for accurate mitosis. In addition, p53 has also been reported to undergo CMA-mediated degradation, resulting in attenuation of p53-dependent signaling [14, 15]. Thus, dysregulated CMA-mediated protein turnover could therefore affect both PCM1-dependent mitotic regulation and p53-dependent senescence.

Histone deacetylase 10 (HDAC10), a class IIb deacetylase, has been implicated in metabolic regulation, autophagy, and DNA-damage-associated processes [16, 17, 18, 19, 20, 21]. HDAC10 has also been linked to HSP70/HSC70-associated macroautophagy regulation, with previous studies reporting an association between HDAC10 activity and the acetylation state of HSP70/HSC70 [17, 18]. Notably, HDAC10 deficiency was shown to enhance CMA in HeLa cells [19]. However, the consequences of this regulation for chromosome stability and cellular senescence remain unclear.

In this study, we investigated how HDAC10 links CMA-dependent protein turnover to chromosome stability and cellular senescence. Our findings support a model in which HDAC10 restrains CMA-dependent turnover of PCM1 and p53, thereby preserving PCM1-dependent mitotic fidelity and p53-dependent senescence, respectively. Our results reveal a functional link between CMA-mediated proteostasis and genome maintenance and suggest that dysregulation of this pathway could contribute to malignant progression in breast cancer.

Materials and Methods

Mouse and cell culture

HDAC10 KO mice (B6N(Cg)-Hdac10tm1.1(KOMP)Mbp/J) were purchased from The Jackson Lab. Animal care and experimentation were conducted in accordance with the guidelines of the Chungnam National University Animal Care and Use Committee (CNU-00540). Mouse embryonic fibroblasts (MEFs) were isolated from embryonic day 14.5 (E14.5) embryos of wild-type (WT) and HDAC10-knockout (KO) mice and subsequently immortalized through continuous passaging. To generate rescue cell lines, HDAC10 KO MEFs were stably transduced with pBABE vectors expressing either wild-type HDAC10 (KO + WT) or a catalytic-dead HDAC10 mutant (KO + CD). Human cervical carcinoma HeLa cells were also used in this study. MEFs and HeLa cells were maintained in Dulbecco's Modified Eagle Medium (DMEM; HyClone, SH30243.01) supplemented with 10% fetal bovine serum (FBS; Gibco, 16000044), 100 U/mL penicillin G, and 100 µg/mL streptomycin (Gibco, 15240-062), and incubated at 37°C in a humidified atmosphere containing 5% CO_2.

Stable cell line generation

Stable rescue MEF cell lines were established by retroviral transduction using pBABE vectors encoding wild-type HDAC10 or a catalytic-dead HDAC10 mutant. Retroviral particles were produced in HEK293T cells by co-transfection of pCL10A1, gag-pol, VSV-G, and the indicated pBABE constructs using polyethylenimine (PEI). Viral supernatants were collected 24 h after transfection, clarified by centrifugation, and used to infect HDAC10 KO MEFs. Stable cell populations were selected with puromycin (1 µg/mL) for 7 days before subsequent experiments.

Chemicals and antibodies

Polyphyllin I (PPD; MedChemExpress, HY-N0047) was dissolved in dimethyl sulfoxide (DMSO) and used at final concentrations of 0.5 or 1 μM for 24 h. Spermidine (Sigma-Aldrich, S0266) was dissolved in sterile distilled water and diluted in DMEM to final concentrations of 10, 50, 100, or 1000 μM for 24 h. Camptothecin (CPT) was used at a final concentration of 2 μM for 24 h. Importazole (MedChemExpress, HY-101091) and Leptomycin B (Santa Cruz Biotechnology, sc-358688) were used at final concentrations of 20 μM and 20 ng/mL, respectively, for 24 h. Nocodazole (Sigma-Aldrich, M1404) was used at a final concentration of 100 ng/mL for cell cycle synchronization and metaphase chromosome spread analysis.

Primary antibodies used in this study included anti-α-tubulin (Santa Cruz Biotechnology, sc-5286), anti-Tom20 (Santa Cruz Biotechnology, sc-11415), anti-Lamin A/C (Santa Cruz Biotechnology, sc-376248), anti-GAPDH (Santa Cruz Biotechnology, sc-32233), anti-RAD51 (Cell Signaling Technology, #8875), anti-γH2AX (Sigma-Aldrich, 05-636), anti-HDAC10 (Merck, H3413), anti-p53 (Merck, OP03), anti-LAMP2A (Cell Signaling Technology, #81197), anti-β-actin (Sigma-Aldrich, AC-74), and anti-PCM1 (Santa Cruz Biotechnology, sc-398365). Alexa Fluor 488-conjugated goat anti-mouse IgG (Jackson ImmunoResearch, 115-545-146) and Rhodamine Red-X-conjugated goat anti-rabbit IgG (Jackson ImmunoResearch, 111-295-144) were used for immunofluorescence staining. HRP-conjugated anti-mouse and anti-rabbit IgG secondary antibodies were used for immunoblotting.

Immunofluorescence staining

For immunofluorescence staining, cells were seeded onto glass coverslips 24 h before the experiment. Cells were fixed with 4% paraformaldehyde for 15 min at room temperature, permeabilized with 0.2% Triton X-100 in phosphate-buffered saline (PBS), and blocked with 5% normal goat serum (NGS). Cells were then incubated overnight at 4°C with the indicated primary antibodies, followed by incubation with Alexa Fluor 488- or Rhodamine Red-X-conjugated secondary antibodies for 1 h at room temperature. Nuclei were counterstained with Hoechst 33342, and coverslips were mounted using ProLong™ Diamond Antifade Mountant (Thermo Fisher Scientific). Fluorescence images were acquired using an Olympus IX71 fluorescence microscope equipped with a Zyla-HF sCMOS camera (Andor Technology). Nuclear area was quantified using ImageJ software, and micronuclei were manually counted from Hoechst-stained images according to established morphological criteria. More than 100 nuclei were analyzed for each experimental group from three independent biological experiments.

Nocodazole synchronization and metaphase chromosome spreading

Cells were cultured until they reached 60–80% confluency and treated with 100 ng/mL nocodazole overnight in a CO_2 incubator at 37°C to induce mitotic arrest. The following day, cells were washed three times with DPBS. For immunofluorescence analysis, the medium was replaced with fresh DMEM, and the cells were released for subsequent analysis. For metaphase chromosome spread analysis, nocodazole-treated cells were collected and incubated with pre-warmed hypotonic solution (0.075 M KCl) at 37°C for 10 min. Following hypotonic treatment, the cells were fixed with ice-cold Carnoy's fixative

(methanol:acetic acid, 3:1). The fixed cell suspension was dropped onto glass slides and dried at 50°C. Chromosomes were stained with Giemsa staining solution (Sigma-Aldrich, 32884) for 10 min at room temperature. The slides were then washed with distilled water, dried, and mounted with synthetic mountant (Thermo Scientific, 6769007). Metaphase chromosome spreads were analyzed by light microscopy.

Western blotting

Whole-cell lysates were prepared in NETN lysis buffer (50 mM Tris-HCl, pH 7.4, 100 mM NaCl, 1 mM EDTA, and 1.0% NP-40) supplemented with protease inhibitor cocktail (1:100), phosphatase inhibitor cocktail (1:100), and dithiothreitol (DTT; 1:1000). Protein concentrations were determined using the Bradford protein assay (Bio-Rad). Equal amounts of protein were separated by SDS-PAGE and transferred onto polyvinylidene difluoride (PVDF) membranes. Membranes were blocked with 5% skim milk in TBST for 1 h at room temperature and incubated overnight at 4°C with the indicated primary antibodies. Following washing with TBST, membranes were incubated with HRP-conjugated secondary antibodies for 1 h at room temperature. Protein bands were visualized using enhanced chemiluminescence (ECL) and imaged using the Fusion Solo 4 imaging system (Vilber Lourmat). Protein band intensities were quantified using ImageJ software (National Institutes of Health, Bethesda, MD, USA) and normalized to GAPDH or β-actin.

LysoTracker staining

Lysosomal content was assessed using LysoTracker™ Red DND-99 (Thermo Fisher Scientific) according to the manufacturer's instructions. Cells were incubated with LysoTracker Red diluted 1:10,000 in complete culture medium for 30 min at 37°C. For fluorescence microscopy, cells were washed with PBS, counterstained with Hoechst 33342, and immediately imaged using an Olympus IX71 fluorescence microscope equipped with a Zyla-HF sCMOS camera. Fluorescence intensity was quantified using MetaMorph software (Molecular Devices). For flow cytometric analysis, LysoTracker-stained cells were harvested by trypsinization, washed with DPBS, and analyzed using a BD Accuri™ C6 Plus flow cytometer (BD Biosciences). At least 5,000 events were acquired for each sample.

Lysosomal activity assay

Lysosomal activity was determined using the Lysosomal Intracellular Activity Assay Kit (Abcam, ab234622) according to the manufacturer's instructions. Briefly, cells were incubated with the self-quenched fluorogenic substrate supplied with the kit. Cytochalasin D provided with the kit was used as an inhibitor control according to the manufacturer's protocol. Fluorescence intensity was analyzed using a BD Accuri™ C6 Plus flow cytometer, and at least 5,000 events were acquired for each sample. Relative lysosomal activity was determined by subtracting the fluorescence intensity of cytochalasin D-treated samples from that of the corresponding untreated samples.

Mouse liver tissue preparation

Liver tissues were obtained from 6-month-old male wild-type (WT) and HDAC10-knockout (KO) mice. For protein extraction, frozen liver tissues were homogenized with beads in RIPA lysis buffer supplemented with protease and phosphatase inhibitors. Following homogenization, tissue lysates were clarified by centrifugation, and the supernatants were collected. Protein concentrations were determined using a bicinchoninic acid (BCA) protein assay. The resulting lysates were subjected to Western blot analysis.

Senescence-associated β-galactosidase (SA-β-gal) assay

Cellular senescence was evaluated using a senescence-associated β-galactosidase (SA-β-gal) staining assay. Cells were fixed with formaldehyde/glutaraldehyde fixation solution for 10–15 min at room temperature and incubated overnight at 37°C in freshly prepared staining solution (pH 6.0) without CO_2. The staining solution contained X-Gal (Bioneer), potassium ferricyanide (III), potassium ferrocyanide (II), and magnesium chloride.

Representative bright-field images were acquired using an Olympus IX71 inverted microscope. For quantitative analysis, the chromogenic product was extracted with 500 μL DMSO per well of a 12-well plate for 10 min on an orbital shaker. Absorbance was measured at 620 nm using a SpectraMax ABS microplate reader (Molecular Devices, San Jose, CA, USA). Absorbance values were used as an indicator of relative SA-β-gal activity.

Kaplan–Meier survival and gene expression correlation analyses

The prognostic significance of HDAC10 expression in breast cancer was evaluated using the publicly available Kaplan–Meier Plotter database. Survival analyses were performed separately using microarray and RNA-sequencing datasets, as these platforms are analyzed independently by Kaplan–Meier Plotter. For the microarray analysis, HDAC10 expression was represented by probe set 226672_s_at. Patients were divided into low- and high-expression groups according to the cutoff applied by the Kaplan–Meier Plotter analysis, and survival curves were generated using the Kaplan–Meier method. Hazard ratios (HRs) with 95% confidence intervals (CIs) and log-rank P values were obtained directly from the database. Numbers of patients at risk were displayed below the survival curves. The Kaplan–Meier Plotter integrates gene-expression and clinical outcome data derived from publicly available datasets, including GEO, EGA, and TCGA, and calculates survival statistics in real time.

The relationship between HDAC10 and LAMP2 transcript expression was assessed using the pair-wise gene expression correlation analysis tool in OncoDB. The breast invasive carcinoma (BRCA) dataset was selected, and HDAC10 and LAMP2 were entered as the genes of interest. RNA-sequencing expression values in OncoDB are normalized as $\log_2$-transformed transcripts per million (TPM). Pearson correlation analysis was used to assess the association between the two genes, and the corresponding correlation coefficient and P value were obtained from the database-generated analysis.

Statistical analysis

All experiments were independently performed at least three times unless otherwise indicated. Quantitative data are presented as the mean ± standard deviation (SD). Statistical analyses were performed using GraphPad Prism version 10 (GraphPad Software, San Diego, CA, USA). Comparisons between two groups were performed using an unpaired two-tailed Student's *t*-test, whereas comparisons among multiple groups were analyzed using one-way analysis of variance (ANOVA). A P value of < 0.05 was considered statistically significant. Statistical significance is indicated as follows: ns, not significant; *$P < 0.05$; **$P < 0.01$; ***$P < 0.001$; and ****$P < 0.0001$.

Results

HDAC10 loss is associated with nuclear enlargement and chromosome instability

To investigate the cellular consequences of HDAC10 loss, we first examined nuclear morphology, mitochondria (Tom20), and tubulin in wild-type (WT) and HDAC10-knockout (HDAC10 KO) mouse embryonic fibroblasts (MEFs). Immunofluorescence staining for Tom20 and α-tubulin revealed no obvious alterations in mitochondrial or microtubule organization, whereas Hoechst staining showed pronounced nuclear enlargement in HDAC10 KO cells compared with WT cells (Fig. 1a). Quantitative analysis demonstrated that both nuclear area and nuclear width were significantly increased following HDAC10 deletion (Fig. 1b). These findings indicate that HDAC10 deficiency is associated with substantial changes in nuclear morphology.

Because nuclear enlargement can accompany alterations in nucleocytoplasmic transport or chromosome content [22, 23, 24], we next examined whether perturbation of nuclear transport differentially affected WT and HDAC10 KO cells. Cells were treated with importazole, an inhibitor of nuclear import, or leptomycin B, an inhibitor of nuclear export, and nuclear size was subsequently assessed (Fig. 1c, d). Both WT and HDAC10 KO cells remained responsive to pharmacological inhibition of nuclear import or export, suggesting that the enlarged nuclear phenotype in HDAC10 KO cells is unlikely to result from a nucleocytoplasmic transport defect.

Given the previously reported involvement of HDAC10 in genome-maintenance pathways [20, 25], we next examined whether HDAC10 deficiency was associated with chromosome-segregation abnormalities. Interestingly, endogenous HDAC10 was enriched in mitotic chromosomes (Supplementary Fig. 1). We next quantified lagging chromosomes during mitosis. HDAC10 KO MEFs showed a marked increase in mitotic cells containing lagging chromosomes, reaching approximately 25% compared with substantially lower levels in WT cells (Fig. 2a, b). Furthermore, metaphase-spread analysis revealed a broader and more heterogeneous chromosome-number distribution in HDAC10 KO cells than in WT cells (Fig. 2c, d). Together, these findings demonstrate that HDAC10 loss is associated with chromosome-segregation defects and increased chromosome-number heterogeneity.

HDAC10 suppresses micronucleus formation

To determine whether the chromosome-segregation abnormalities observed in HDAC10 KO cells were accompanied by defective partitioning of chromosomal material, we next examined micronucleus formation in WT and HDAC10 KO MEFs. Immunofluorescence staining revealed extranuclear DNA-containing structures surrounded by lamin, consistent with micronuclei (Fig. 3a). The frequency of micronucleated cells was significantly increased in HDAC10 KO MEFs compared with WT cells (Fig. 3b). Together with the increased occurrence of lagging chromosomes and chromosome-number heterogeneity, these findings indicate that HDAC10 deficiency is associated with impaired chromosome stability. Re-expression of wild-type HDAC10 markedly reduced the frequency of micronucleated cells compared with HDAC10 KO cells (Fig. 3c, d). In contrast, the catalytically inactive mutant was significantly less effective than wild-type HDAC10 in suppressing micronucleus formation (Fig. 3c, d). These results indicate that the catalytic activity of HDAC10 contributes substantially to the maintenance of chromosome stability and the suppression of micronucleus formation.

HDAC10 deficiency increases LAMP2A expression and lysosomal activity

Chaperone-mediated autophagy (CMA) selectively regulates protein turnover and has been implicated in the control of DNA-damage-response proteins [10]. Previous studies have linked HDAC10 to HSP70/HSC70-associated autophagy regulation [17, 18] and CMA-associated substrate degradation following HDAC10 knockout in HeLa cells [19]. To investigate the role of HDAC10 on CMA. we first examined LAMP2A, the CMA receptor [9]. Immunoblot analysis showed that LAMP2A protein levels were markedly increased in HDAC10 KO MEFs compared with WT cells (Fig. 4a, b).

We next examined whether HDAC10 deficiency was associated with broader alterations in lysosome. LysoTracker staining revealed no significant difference in overall lysosomal structure and abundance between WT and HDAC10 KO MEFs (Fig. 4c, d). In contrast, lysosomal proteolytic activity was significantly increased in HDAC10 KO cells (Fig. 4e). Thus, HDAC10 deficiency enhanced lysosomal degradative activity despite the absence of a detectable change in overall lysosome structure and abundance. Restoration of wild-type HDAC10 markedly reduced LAMP2A levels toward those observed in WT cells, whereas the catalytically inactive mutant was significantly less effective in suppressing LAMP2A expression (Fig. 4f, g). These findings indicate that HDAC10 catalytic activity contributes to the regulation of LAMP2A.

HDAC10 functions as an N^8-acetylspermidine deacetylase[21, 26, 27], generating spermidine through polyamine deacetylation. Therefore, we next asked whether altered polyamine metabolism could account for the increase in LAMP2A. Treatment with exogenous spermidine over a concentration range of 10–1000 μM did not produce an apparent change in LAMP2A protein levels in either WT or HDAC10 KO MEFs (Supplementary Fig. 2). These results suggest that the increase in LAMP2A associated with HDAC10 deficiency cannot be explained by reduced spermidine availability. To get physiological

importance, we examined LAMP2A in liver tissue from 6-month-old WT and HDAC10 KO mice. Importantly, LAMP2A protein levels were significantly increased in HDAC10 KO liver compared with WT liver (Fig. 4h, i).

HDAC10 preserves PCM1 by limiting its CMA-dependent degradation.

PCM1 has been identified as a substrate of DNAJA2–HSC70-dependent chaperone-mediated autophagy (CMA), and dysregulation of PCM1 turnover has been shown to increase micronucleus formation [11]. These observations prompted us to investigate whether altered PCM1 turnover provides a mechanistic link between enhanced CMA-associated regulation and chromosome instability in HDAC10-deficient cells.

Immunoblot analysis revealed a marked reduction in PCM1 protein levels in HDAC10 KO MEFs compared with WT cells (Fig. 5a). Quantification showed that PCM1 was reduced to approximately 30% of the WT level (Fig. 5b). Re-expression of wild-type HDAC10 substantially restored PCM1 protein levels, whereas the catalytically inactive mutant was significantly less effective in restoring PCM1 (Fig. 5c, d). These findings indicate that HDAC10 catalytic activity is important for maintaining PCM1 protein levels.

We next examined whether the reduction in PCM1 following HDAC10 loss resulted from enhanced CMA-dependent turnover. WT and HDAC10 KO MEFs were treated with polyphyllin D (PPD), a pharmacological inhibitor of CMA [28]. PPD treatment increased PCM1 protein abundance in HDAC10KO cells, with a clear recovery observed at 1 μM PPD (Fig. 5e). This restoration of PCM1 following CMA inhibition supports the involvement of enhanced CMA-dependent degradation of PCM1 caused by HDAC10 deficiency.

To determine whether enhanced CMA also contributes to the chromosome-instability phenotype of HDAC10-deficient cells, we examined micronucleus formation following PPD treatment. Notably, treatment of HDAC10 KO cells with 1 μM PPD significantly reduced micronucleus formation (Fig. 5f, g), indicating that excessive CMA activity contributes to this phenotype. Together, these results suggested that excessive CMA-dependent turnover of PCM1 contributes to the maintenance of chromosome stability.

HDAC10 preserves p53 by limiting its CMA-dependent degradation.

To investigate the relationship between HDAC10 and the DNA-damage response, we first examined its subcellular localization following genotoxic stress. Treatment of HeLa cells expressing HDAC10–GFP with camptothecin (CPT; 2 μM) increased the nuclear accumulation of HDAC10 compared with untreated cells (Supplementary Fig. 3). These findings indicate that HDAC10 undergoes redistribution toward the nucleus in response to genotoxic stress.

We next examined whether HDAC10 deficiency was associated with altered DNA-damage responses. Immunoblot analysis of WT and HDAC10 KO MEFs at passages 25 and 49 revealed increased levels of the DNA-damage-associated marker γH2AX and the homologous recombination protein RAD51 in

HDAC10 KO cells, with the most pronounced changes observed at passage 49 (Fig. 6a) indicating that HDAC10 loss is accompanied by enhanced DNA-damage-associated signaling, particularly during prolonged culture.

Because p53 is a major mediator of cellular responses to DNA damage [6] and another CMA substrate [14, 15], we next examined whether its abundance was altered by HDAC10 deficiency. Despite the increased DNA-damage-associated signals, p53 protein levels were markedly reduced in HDAC10 KO MEFs to approximately 50% of those in WT cells (Fig. 6b, c). Re-expression of wild-type HDAC10 substantially restored p53, whereas the catalytically inactive HDAC10 mutant was significantly less effective (Fig. 6c).

Given the increased LAMP2A expression and lysosomal activity observed following HDAC10 loss, we therefore examined whether CMA inhibition could restore p53 in HDAC10 KO cells. WT and HDAC10 KO MEFs were treated with the CMA inhibitor polyphyllin D (PPD; 0.5 or 1 μM). PPD treatment increased p53 protein abundance in HDAC10 KO cells compared with untreated KO cells, with a clear recovery observed at 1 μM PPD (Fig. 6d). This pharmacological restoration of p53 is consistent with enhanced CMA-dependent turnover contributing to the reduction of p53 following HDAC10 loss. Together, HDAC10 deficiency is associated with increased DNA-damage signaling but reduced p53, potentially uncoupling the accumulation of genomic stress from an appropriate p53-dependent cellular response.

HDAC10 promotes senescence-associated responses to high-density culture and genotoxic stress

Given the increased DNA-damage-associated signaling and reduced p53 observed in HDAC10 KO MEFs, we next examined whether HDAC10 deficiency affected senescence-associated responses. WT and HDAC10 KO MEFs were maintained under prolonged high-density culture conditions for one week and subsequently assessed for senescence-associated β-galactosidase (SA-β-gal) activity. WT cells exhibited prominent SA-β-gal staining, whereas HDAC10 KO cells showed markedly weaker staining (Fig. 7a). Quantification confirmed that relative SA-β-gal activity in HDAC10 KO MEFs was reduced to approximately 45% of that observed in WT cells (Fig. 7b). These findings indicate that HDAC10 deficiency attenuates the senescence-associated response despite of DNA damages

To determine whether the catalytic activity of HDAC10 contributes to this phenotype, we compared WT, HDAC10 KO, KO + WT, and KO + CD MEFs under different cell-density conditions. At a lower seeding density (2.5×10^5 cells), all four groups exhibited relatively weak SA-β-gal staining after 24 h (Fig. 7c). In contrast, at high seeding density (1×10^6 cells), WT cells exhibited a stronger SA-β-gal response, whereas HDAC10 KO cells showed reduced staining. Re-expression of wild-type HDAC10 enhanced SA-β-gal staining in HDAC10 KO cells, whereas the catalytically inactive mutant was less effective (Fig. 7d). These observations suggest that HDAC10 catalytic activity contributes to the senescence-associated response under high-density culture conditions.

We next examined whether HDAC10 similarly influenced the response to genotoxic stress. Following UV exposure for 10 s, cells were cultured for an additional 24 h and subjected to SA-β-gal staining. WT and KO + WT cells exhibited more pronounced SA-β-gal staining than HDAC10 KO and KO + CD cells (Fig. 7e), suggesting a role for HDAC10 in promoting senescence-associated responses that limit the propagation of genomically damaged cells.

To determine whether enhanced CMA contributes to the attenuated senescence-associated response in HDAC10-deficient cells, we next examined the effect of pharmacological CMA inhibition. Treatment of HDAC10 KO MEFs with polyphyllin D (PPD; 1 μM) significantly increased SA-β-gal activity compared with untreated HDAC10 KO cells, although the response remained below that observed in WT cells (Fig. 7f, g). The partial restoration of SA-β-gal activity following CMA inhibition indicates that enhanced CMA contributes to the impaired senescence-associated response caused by HDAC10 deficiency. Together, these results support a model in which dysregulated CMA contributes to attenuation of the p53-dependent senescence following HDAC10 loss. This impaired senescence response in HDAC10 KO cells allows genomically damaged cells to continue proliferating.

Clinical associations of HDAC10 and LAMP2 expression in breast cancer

Because our findings linked HDAC10-dependent regulation of CMA-associated proteostasis to chromosome stability and cellular senescence, we next examined the potential clinical relevance of this pathway in breast cancer. Breast cancer was selected because chromosomal instability and frequent TP53 alterations are prominent features of the disease [29, 30], providing a relevant context in which to examine pathways involved in genome maintenance and stress-responsive cell-fate control.

We first analyzed the association between HDAC10 expression and patient survival using microarray and RNA-sequencing datasets available through Kaplan–Meier Plotter. In the microarray dataset, higher HDAC10 expression was associated with significantly more favorable survival than lower expression (Fig. 8a). A concordant association was observed in the RNA-sequencing dataset (Fig. 8b). We next examined the relationship between HDAC10 and LAMP2 expression in the breast invasive carcinoma (BRCA) dataset using OncoDB (https://oncodb.org). Pearson correlation analysis of $\log_2$-transformed transcripts per million (TPM) revealed a significant inverse correlation between HDAC10 and LAMP2 expression (Fig. 8c). These analyses therefore associated higher HDAC10 expression with favorable survival and identified an inverse relationship between HDAC10 and LAMP2 in breast cancer.

We next examined whether HDAC10 and LAMP2 expression were associated with pathological response to anthracycline-based chemotherapy, using public transcriptome database (https://rocplot.com). Anthracyclines were selected because they induce DNA damage and can elicit sustained DNA-damage responses, including cellular senescence [31]. ROC plot analysis included 507 breast cancer patients, comprising 119 responders and 388 non-responders. HDAC10 expression was numerically higher in responders than in non-responders. ROC analysis showed a modest but significant association between HDAC10 expression and pathological response (Supplementary Fig. 4). In contrast, LAMP2 expression

was lower in responders than in non-responders (Supplementary Fig. 5). This difference was significant by the Mann–Whitney test (P = 0.0271), and ROC analysis likewise showed a modest but significant association between LAMP2 expression and pathological response (Supplementary Fig. 5). Thus, responders exhibited a reciprocal expression pattern characterized by relatively higher HDAC10 and lower LAMP2 expression.

Based on our findings, we propose a model in which HDAC10 coordinates chromosome stability and cellular senescence through regulation of CMA-associated protein turnover (Fig. 8). In wild-type cells, HDAC10 restrains excessive CMA activity and maintains appropriate LAMP2A abundance, thereby preserving PCM1 and p53 protein levels. Thus, HDAC10 loss creates a dual defect in cancer cells by simultaneously impairing PCM1-dependent chromosome segregation and p53-dependent senescence, thereby promoting both the generation and persistence of genomic instability.

Discussion

Maintenance of genome integrity requires coordinated control of chromosome segregation [2, 4], protein homeostasis [32], and cellular responses to genomic stress [1]. In this study, we identify HDAC10 as a regulator linking CMA-associated proteostasis to genome stability and cellular senescence. HDAC10 loss increased LAMP2A and lysosomal activity, reduced PCM1 and p53, and was accompanied by chromosome instability and impaired senescence-associated responses. These findings support a model in which HDAC10 limits excessive CMA-dependent turnover of PCM1 and p53, thereby coordinating PCM1-dependent mitotic fidelity with p53-dependent senescence to restrict both the generation and persistence of genomic instability.

Nuclear enlargement was a prominent phenotype associated with HDAC10 deficiency. Although increased nuclear size can arise from several mechanisms, including alterations in nucleocytoplasmic transport and nuclear architecture [33], our data suggest that chromosome instability contribute substantially to this phenotype. HDAC10 deficient cells exhibited increased lagging chromosomes, broader chromosome-number distributions, and elevated micronucleus formation, indicating persistent errors in chromosome segregation. Changes in chromosome content and aneuploidy can alter nuclear volume and organization [23, 24], and repeated segregation errors therefore contribute to the enlarged and heterogeneous nuclear morphology observed in HDAC10 KO cells. Importantly, pharmacological perturbation of nuclear import or export did not selectively reproduce or normalize the HDAC10-dependent phenotype, arguing against a nucleocytoplasmic transport defect as the primary explanation. Thus, we propose that nuclear enlargement in HDAC10-deficient cells likely reflects the cumulative consequences of chromosome-number abnormalities and disrupted nuclear organization associated with genomic instability.

Spermidine is known to stimulate macroautophagy [34], but whether it directly regulates CMA remains unclear. HDAC10 is a major N^8-acetylspermidine deacetylase [26], raising the possibility that loss of HDAC10 might activate CMA through the reduction of intracellular spermidine availability. However,

spermidine supplementation failed to reverse the increase in LAMP2A observed in HDAC10 KO cells, arguing against a model in which reduced spermidine activates CMA. Instead, our catalytic activity dependent rescue data support the existence of an additional HDAC10-dependent mechanism that regulates CMA-associated lysosomal proteostasis. Previous studies linking HDAC10 to HSP70/HSC70-associated macroautophagy and altered HSP70/HSC70 acetylation [17, 18] raise the possibility that HDAC10 influence CMA through regulation of chaperone function, substrate handling, or LAMP2A-dependent lysosomal delivery. Thus, further studies identifying the relevant HDAC10 target(s) and defining how HDAC10 catalytic activity regulates the CMA machinery will be important.

Our findings support a cooperative model in which PCM1 and p53 act at distinct but complementary levels to protect genome stability as a downstream of HDAC10. PCM1 primarily contributes to the prevention of genomic abnormalities by supporting centriolar satellite function, mitotic fidelity, and accurate chromosome segregation [12, 13], whereas p53 provides a second protective barrier by promoting senescence when genomic instability has already occurred [8]. In HDAC10 deficient cells, the simultaneous reduction of PCM1 and p53 by CMA therefore compromise both layers of genome protection: decreased PCM1 increase the generation of chromosome-segregation errors and micronuclei, while reduced p53 weaken the growth-restrictive senescence of genomically abnormal cells. Because CMA inhibition restored both PCM1 and p53, these observations suggest that HDAC10 coordinates these two protective pathways through the regulation of CMA. Loss of HDAC10 could therefore create a dual defect in which chromosome abnormalities are generated more frequently and cells carrying these abnormalities are less effectively restrained, potentially important for promoting tumor heterogeneity and malignant progression in cancer.

Breast cancer provides a particularly relevant model in which to examine the consequences of genomic instability because chromosome instability, aneuploidy, and TP53 alterations are common features of the disease and can contribute to tumor heterogeneity and progression [30, 35, 36]. In this context, the dual genome-protective role of HDAC10 be especially important. Across public datasets, higher HDAC10 was associated with favorable survival and showed an inverse relationship with LAMP2. In anthracycline-treated patients, responders also exhibited relatively higher HDAC10 and lower LAMP2 expression, a pattern consistent with our model linking HDAC10 to restrained CMA-associated proteostasis and improved responses to genotoxic stress. Although these associations are correlative and have limited predictive strength, they suggest that dysregulation of the HDAC10–CMA axis have clinical relevance in breast cancer progression and treatment response.

In conclusion, HDAC10 protects genome stability through two complementary mechanisms by limiting CMA-dependent degradation of PCM1 and p53. Thus, HDAC10 loss creates a dual defect by simultaneously impairing PCM1-dependent chromosome segregation and p53-dependent senescence, thereby promoting both the generation and persistence of genomic instability. This dual impairment would contribute to tumor heterogeneity and malignant progression in cancer.

Abbreviations

CMA
Chaperone-Mediated Autophagy
CPT
Camptothecin
DNAJA2
DnaJ Heat Shock Protein Family (Hsp40) Member A2
HDAC10
Histone Deacetylase 10
HSC70
Heat Shock Cognate 70
HSP70
Heat Shock Protein 70
LAMP2A
Lysosome-Associated Membrane Protein Type 2A
MEF
Mouse Embryonic Fibroblast
PCM1
Pericentriolar Material 1
PPD
Polyphyllin D (Polyphyllin I)
p53
Tumor Protein p53
RAD51
RAD51 Recombinase
SA-β-gal
Senescence-Associated β-Galactosidase
γH2AX
Phosphorylated Histone H2AX

Declarations

Conflict of Interest:

The authors declare that they have no conflict of interest.

Ethics approval and consent to participate

Animal care and experimentation were conducted in accordance with the guidelines of the Chungnam National University Animal Care and Use Committee (CNU-00540).

Funding

This work was supported by the National Research Foundation of Korea (RS-2025-16065072, RS-2025-02215209, RS-2025-25442707, RS-2026-25565351 and Chungnam National University).

Authors' contributions

U.K. and K.S. contributed equally to this work. J.Y.L. conceived and designed the study. U.K., K.S., M.K., D.U.K., M.H.V., and J.K. performed experiments and analyzed the data. U.K. K.S. and J.Y.L. wrote the manuscript with input from all authors. J.Y.L. supervised the study. All authors reviewed and approved the final manuscript.

Acknowledgements

We thank Dr. Hwan-Woo Park for critical reading. This work was supported by the National Research Foundation of Korea (RS-2025-16065072, RS-2025-02215209, RS-2025-25442707, RS-2026-25565351 and Chungnam National University.

Availability of data and materials:

Not applicable.

References

1. Groelly FJ, Fawkes M, Dagg RA, Blackford AN, Tarsounas M. Targeting DNA damage response pathways in cancer. *Nat Rev Cancer* 2023, **23**(2): 78–94.
2. Devillers R, Dos Santos A, Destombes Q, Laplante M, Elowe S. Recent insights into the causes and consequences of chromosome mis-segregation. *Oncogene* 2024, **43**(43): 3139–3150.
3. Crasta K, Ganem NJ, Dagher R, Lantermann AB, Ivanova EV, Pan Y, *et al.* DNA breaks and chromosome pulverization from errors in mitosis. *Nature* 2012, **482**(7383): 53–58.
4. Santaguida S, Amon A. Short- and long-term effects of chromosome mis-segregation and aneuploidy. *Nat Rev Mol Cell Biol* 2015, **16**(8): 473–485.
5. Abuetabh Y, Wu HH, Chai C, Al Yousef H, Persad S, Sergi CM, *et al.* DNA damage response revisited: the p53 family and its regulators provide endless cancer therapy opportunities. *Exp Mol Med* 2022, **54**(10): 1658–1669.
6. Kastenhuber ER, Lowe SW. Putting p53 in Context. *Cell* 2017, **170**(6): 1062–1078.
7. Dirac AM, Bernards R. Reversal of senescence in mouse fibroblasts through lentiviral suppression of p53. *J Biol Chem* 2003, **278**(14): 11731–11734.

8. Mijit M, Caracciolo V, Melillo A, Amicarelli F, Giordano A. Role of p53 in the Regulation of Cellular Senescence. *Biomolecules* 2020, **10**(3).
9. Kaushik S, Cuervo AM. Chaperone-mediated autophagy: a unique way to enter the lysosome world. *Trends Cell Biol* 2012, **22**(8): 407–417.
10. Park C, Suh Y, Cuervo AM. Regulated degradation of Chk1 by chaperone-mediated autophagy in response to DNA damage. *Nat Commun* 2015, **6**: 6823.
11. Huang Y, Lu C, Wang H, Gu L, Fu YX, Li GM. DNAJA2 deficiency activates cGAS-STING pathway via the induction of aberrant mitosis and chromosome instability. *Nat Commun* 2023, **14**(1): 5246.
12. Begar E, Seyrek E, Firat-Karalar EN. Navigating centriolar satellites: the role of PCM1 in cellular and organismal processes. *FEBS J* 2025, **292**(4): 688–708.
13. Holdgaard SG, Cianfanelli V, Pupo E, Lambrughi M, Lubas M, Nielsen JC, *et al.* Selective autophagy maintains centrosome integrity and accurate mitosis by turnover of centriolar satellites. *Nat Commun* 2019, **10**(1): 4176.
14. Vakifahmetoglu-Norberg H, Kim M, Xia HG, Iwanicki MP, Ofengeim D, Coloff JL, *et al.* Chaperone-mediated autophagy degrades mutant p53. *Genes Dev* 2013, **27**(15): 1718–1730.
15. Aydin Y, Chatterjee A, Chandra PK, Chava S, Chen W, Tandon A, *et al.* Interferon-alpha-induced hepatitis C virus clearance restores p53 tumor suppressor more than direct-acting antivirals. *Hepatol Commun* 2017, **1**(3): 256–269.
16. Kao HY, Lee CH, Komarov A, Han CC, Evans RM. Isolation and characterization of mammalian HDAC10, a novel histone deacetylase. *J Biol Chem* 2002, **277**(1): 187–193.
17. Oehme I, Linke JP, Böck BC, Milde T, Lodrini M, Hartenstein B, *et al.* Histone deacetylase 10 promotes autophagy-mediated cell survival. *Proc Natl Acad Sci U S A* 2013, **110**(28): E2592-2601.
18. Lai IL, Lin TP, Yao YL, Lin CY, Hsieh MJ, Yang WM. Histone deacetylase 10 relieves repression on the melanogenic program by maintaining the deacetylation status of repressors. *J Biol Chem* 2010, **285**(10): 7187–7196.
19. Obayashi H, Nagano Y, Takahashi T, Seki T, Tanaka S, Sakai N, *et al.* Histone deacetylase 10 knockout activates chaperone-mediated autophagy and accelerates the decomposition of its substrate. *Biochem Biophys Res Commun* 2020, **523**(1): 246–252.
20. Kotian S, Liyanarachchi S, Zelent A, Parvin JD. Histone deacetylases 9 and 10 are required for homologous recombination. *J Biol Chem* 2011, **286**(10): 7722–7726.
21. Hai Y, Shinsky SA, Porter NJ, Christianson DW. Histone deacetylase 10 structure and molecular function as a polyamine deacetylase. *Nat Commun* 2017, **8**: 15368.
22. Kume K, Cantwell H, Neumann FR, Jones AW, Snijders AP, Nurse P. A systematic genomic screen implicates nucleocytoplasmic transport and membrane growth in nuclear size control. *PLoS Genet* 2017, **13**(5): e1006767.
23. Kemeny S, Tatout C, Salaun G, Pebrel-Richard C, Goumy C, Ollier N, *et al.* Spatial organization of chromosome territories in the interphase nucleus of trisomy 21 cells. *Chromosoma* 2018, **127**(2):

247–259.

24. Hwang S, Williams JF, Kneissig M, Lioudyno M, Rivera I, Helguera P, *et al.* Suppressing Aneuploidy-Associated Phenotypes Improves the Fitness of Trisomy 21 Cells. *Cell Rep* 2019, **29**(8): 2473–2488 e2475.
25. Radhakrishnan R, Li Y, Xiang S, Yuan F, Yuan Z, Telles E, *et al.* Histone deacetylase 10 regulates DNA mismatch repair and may involve the deacetylation of MutS homolog 2. *J Biol Chem* 2015, **290**(37): 22795–22804.
26. Stewart TM, Foley JR, Holbert CE, Klinke G, Poschet G, Steimbach RR, *et al.* Histone deacetylase-10 liberates spermidine to support polyamine homeostasis and tumor cell growth. *J Biol Chem* 2022, **298**(10): 102407.
27. Herbst-Gervasoni CJ, Steimbach RR, Morgen M, Miller AK, Christianson DW. Structural Basis for the Selective Inhibition of HDAC10, the Cytosolic Polyamine Deacetylase. *ACS Chem Biol* 2020, **15**(8): 2154–2163.
28. Dong RF, Qin CJ, Yin Y, Han LL, Xiao CM, Wang KD, *et al.* Discovery of a potent inhibitor of chaperone-mediated autophagy that targets the HSC70-LAMP2A interaction in non-small cell lung cancer cells. *Br J Pharmacol* 2025, **182**(10): 2287–2309.
29. Cancer Genome Atlas N. Comprehensive molecular portraits of human breast tumours. *Nature* 2012, **490**(7418): 61–70.
30. Kim R, Yu J, Lim J, Oh BB, Nam SJ, Kim SW, *et al.* Whole-genome landscapes of 1,364 breast cancers. *Nature* 2026, **649**(8099): 1282–1291.
31. Seara FAC, Kasai-Brunswick TH, Nascimento JHM, Campos-de-Carvalho AC. Anthracycline-induced cardiotoxicity and cell senescence: new therapeutic option? *Cell Mol Life Sci* 2022, **79**(11): 568.
32. Kaushik S, Cuervo AM. The coming of age of chaperone-mediated autophagy. *Nat Rev Mol Cell Biol* 2018, **19**(6): 365–381.
33. Prabha H, Phan P, Levy DL. Getting nuclear size just right - emerging mechanisms regulating nuclear scaling and morphology. *J Cell Sci* 2026, **139**(12).
34. Eisenberg T, Knauer H, Schauer A, Buttner S, Ruckenstuhl C, Carmona-Gutierrez D, *et al.* Induction of autophagy by spermidine promotes longevity. *Nat Cell Biol* 2009, **11**(11): 1305–1314.
35. Chen X, Agustinus AS, Li J, DiBona M, Bakhoum SF. Chromosomal instability as a driver of cancer progression. *Nat Rev Genet* 2025, **26**(1): 31–46.
36. Ben-David U, Amon A. Context is everything: aneuploidy in cancer. *Nat Rev Genet* 2020, **21**(1): 44–62.

Figures

Figure 1.

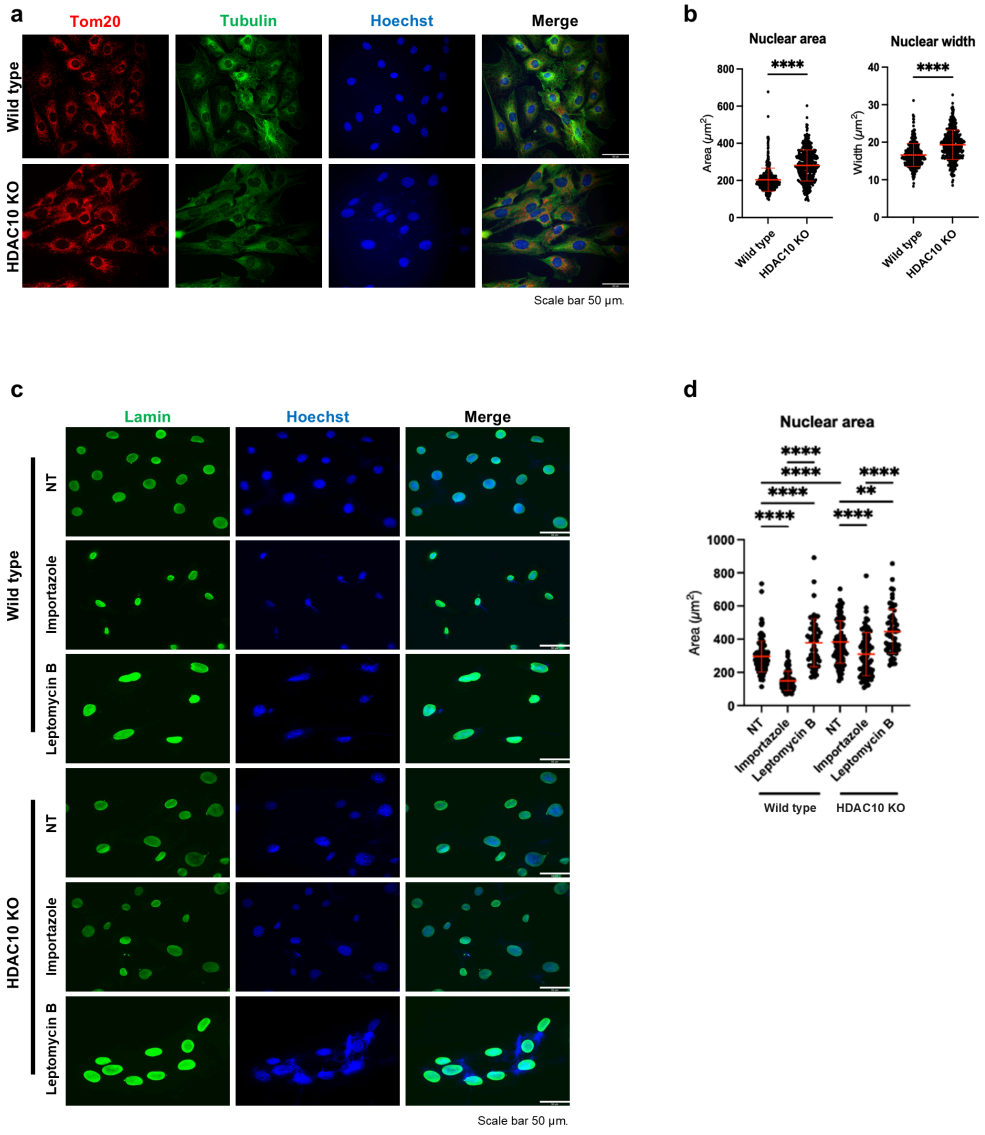

Figure 1

HDAC10 deficiency induces nuclear enlargement.

a Representative immunofluorescence images of wild-type (WT) and HDAC10-knockout (KO) mouse embryonic fibroblasts (MEFs) stained for TOM20 (red), α-tubulin (green), and DNA (Hoechst; blue). **b** Quantification of nuclear area and width in WT and KO MEFs; more than 400 nuclei were analyzed. **c**

Representative immunofluorescence images of WT and KO MEFs following treatment with the nuclear-import inhibitor importazole or the nuclear-export inhibitor leptomycin B. Cells were stained for lamin (green) and DNA (Hoechst; blue). NT, untreated. **d** Quantification of nuclear area under the conditions shown in **c**; more than 50 nuclei were analyzed. Data are presented as mean ± SD. ***P* < 0.01; *****P* < 0.0001, for the indicated comparisons. (Scale bars, 50 μm.)

Figure 2.

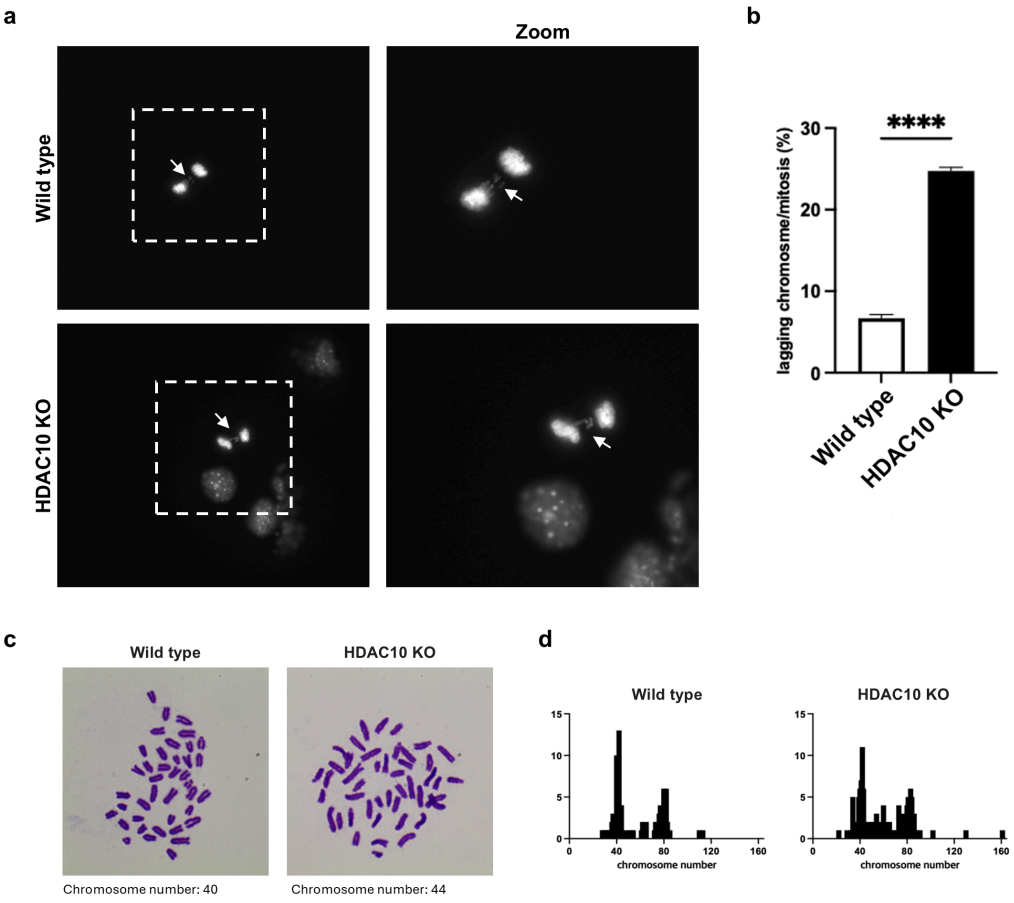

Figure 2

HDAC10 deficiency increases lagging chromosomes and chromosome-number heterogeneity.

a Representative image of mitotic WT and HDAC10 KO MEFs stained with Hoechst to visualize DNA. White arrows indicate lagging chromosomes. Boxed regions are enlarged in the adjacent panels. **b** Percentage of mitotic cells exhibiting lagging chromosomes; more than 100 mitotic cells were analyzed in each 3 independent experiments and presented as mean ± SD. ****$P < 0.0001$. **c** Representative metaphase chromosome spreads from WT and KO MEFs. Chromosome counts for the illustrated spreads are indicated. **d** Distribution of chromosome numbers in WT and KO MEFs; more than 100 metaphase spreads were analyzed.

Figure 3.

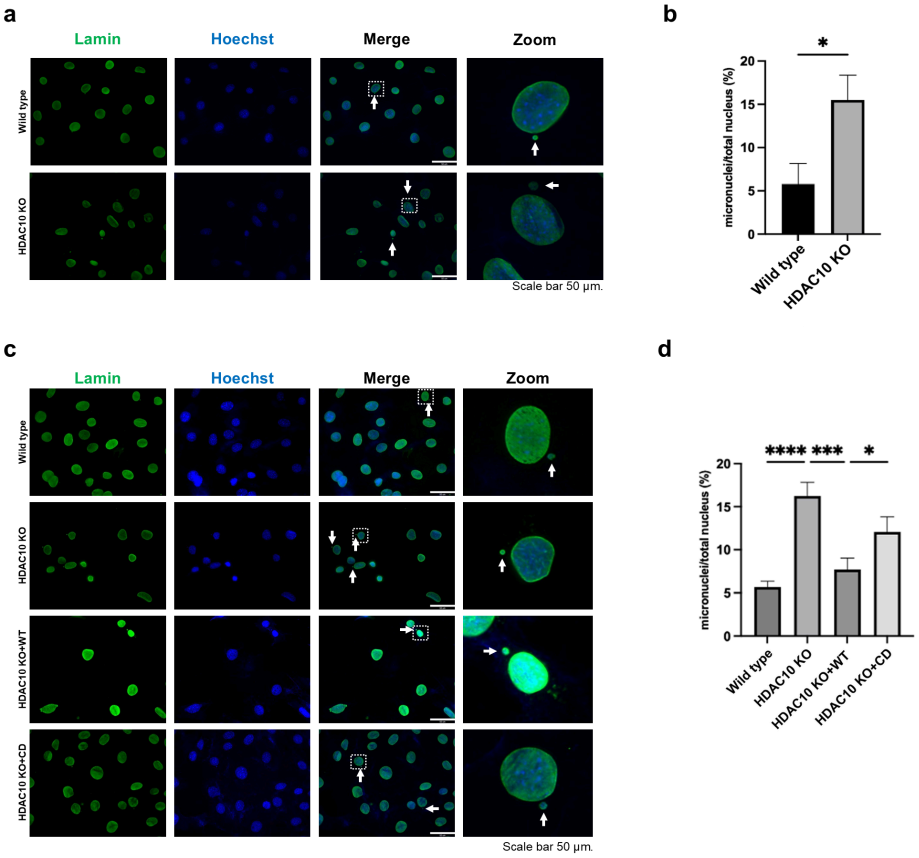

Figure 3

HDAC10 inhibits micronucleus formation.

a Representative immunofluorescence images of WT and HDAC10 KO MEFs stained for lamin (green) and DNA (Hoechst; blue). White arrows indicate micronuclei, and boxed regions are enlarged in the adjacent panels. (Scale bar, 50 μm.) **b** Quantification of micronuclei relative to the total number of nuclei

in **a.** More than 100 nuclei were analyzed in each experiment. Data are presented as mean of 3 independent experiments with ± SD. *P < 0.05. **c** Representative images of WT, KO, KO cells reconstituted with wild-type HDAC10 (KO+WT), and a catalytically inactive HDAC10 mutant (KO+CD), stained as in **a**. **d** Quantification of micronuclei relative to total nuclei in the groups shown in **c**. More than 100 nuclei were analyzed for each experiment. Data are presented as mean of 3 independent experiments with ± SD. *P < 0.05; ***P < 0.001; ****P < 0.0001, for the indicated comparisons.

Figure 4.

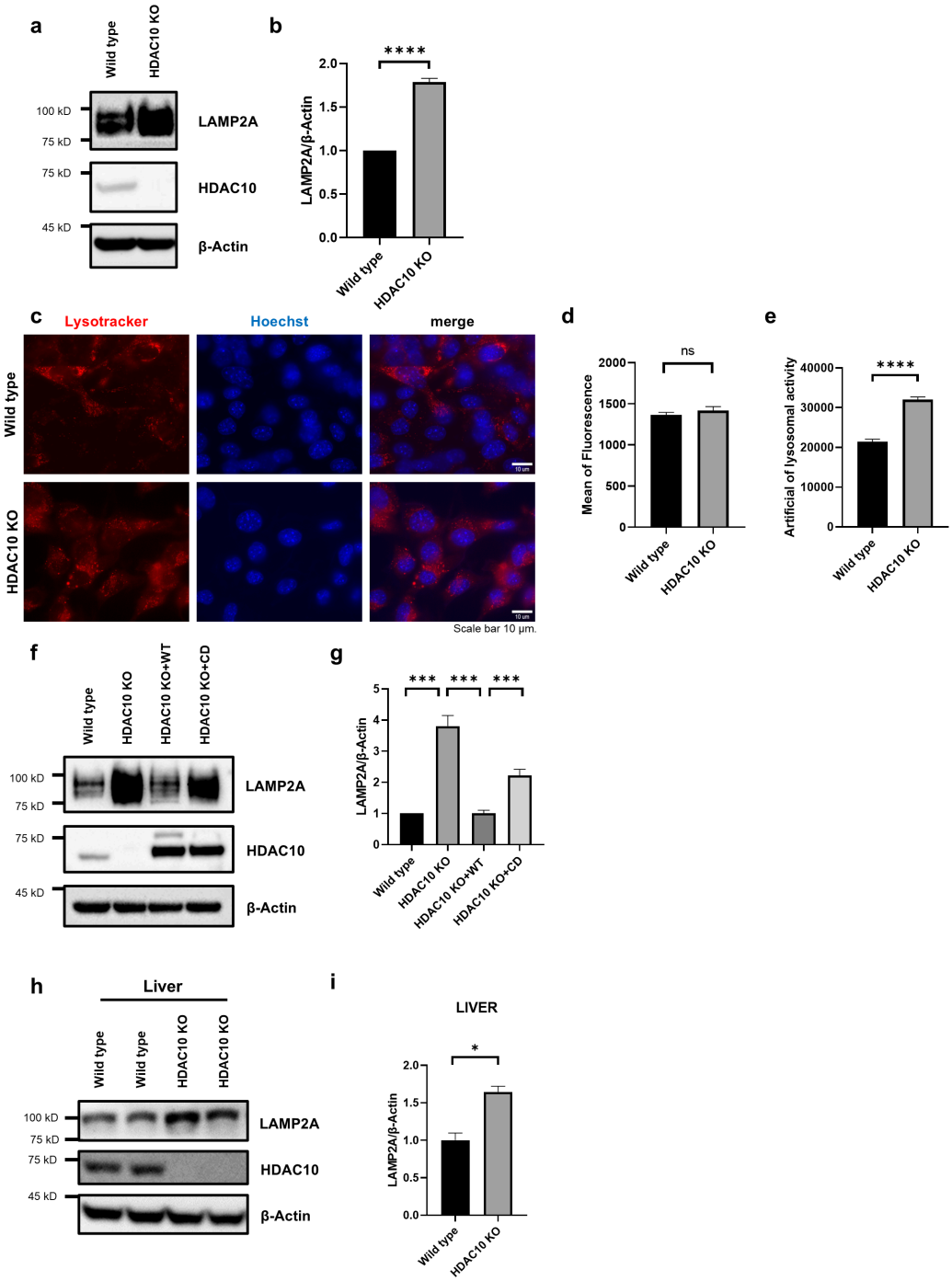

Figure 4

CMA is suppressed by HDAC10 deacetylase activity.

a Representative immunoblots of LAMP2A and HDAC10 in WT and HDAC10 KO MEFs. β-Actin served as the loading control. **b** Densitometric quantification of LAMP2A normalized to β-actin. Data are presented as a mean of 3 independent experiments with ±SD. ****P < 0.0001. **c** Representative fluorescence images of WT and KO MEFs stained with LysoTracker Red and Hoechst (blue). (Scale bar, 10 μm). **d** Quantification of LysoTracker fluorescence intensity was presented as mean of fluorescence intensity. Data are presented as a mean of 3 independent experiments with ±SD. (N.S. not significant). **e** Relative lysosomal activity measured using a self-quenched fluorogenic substrate and flow cytometry. At least 5,000 events were acquired per sample. Activity was calculated by subtracting the fluorescence intensity of cytochalasin D–treated controls from that of the corresponding untreated samples. Data are presented as a mean of 3 independent experiments with ±SD. ****P < 0.0001.**f** Representative immunoblots of LAMP2A and HDAC10 in WT, KO, KO+WT, and KO+CD MEFs. **g** Quantification of LAMP2A normalized to β-actin in **f**. Data are presented as mean of 3 independent experiments ± SD. ***P < 0.001. **h** Representative immunoblots of LAMP2A and HDAC10 in liver tissue from 6-month-old WT and HDAC10 KO mice. **i** Quantification of hepatic LAMP2A normalized to β-actin. Data are presented as mean of 2 independent mouse liver samples ± SD. *P < 0.05.

Figure 5.

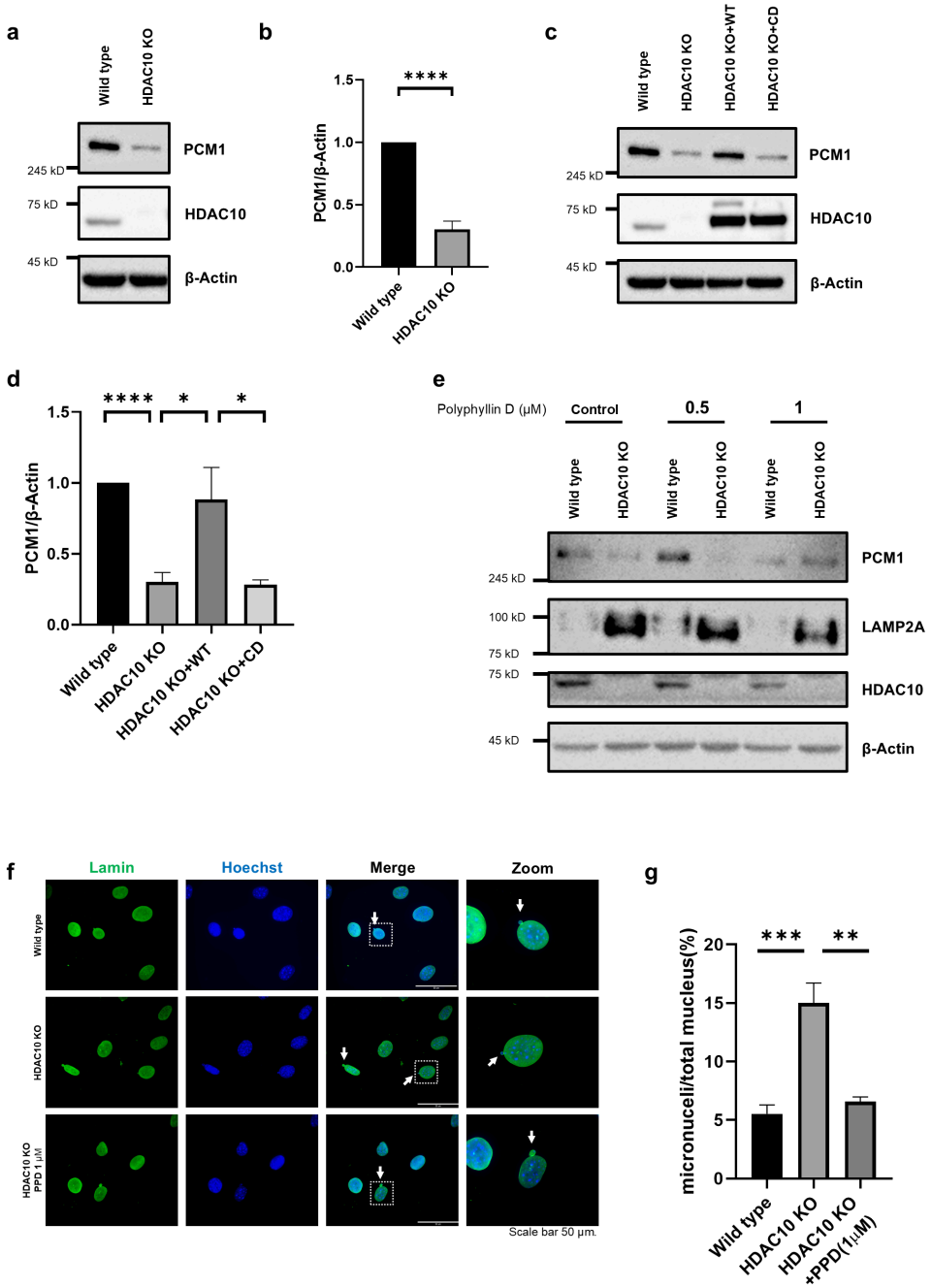

Figure 5

HDAC10 suppresses CMA to maintain PCM1

a Representative immunoblots of PCM1 and HDAC10 in WT and HDAC10 KO MEFs. **b** Densitometric quantification of PCM1 normalized to β-actin. Data are presented as a mean of 3 independent experiments with ±SD. ****$P < 0.0001$. **c** Representative immunoblots of PCM1 and HDAC10 in WT, KO,

KO+WT, and KO+CD MEFs. **d** Quantification of PCM1 normalized to β-actin in **c**. Data are presented as a mean of 3 independent experiments with ±SD. *P < 0.05; ****P < 0.0001, for the indicated comparisons. **e** Representative immunoblots of PCM1, LAMP2A, and HDAC10 in WT and KO MEFs treated with polyphyllin D (PPD; 0.5 or 1 μM) or maintained under control conditions. β-Actin served as the loading control. **f** Representative immunofluorescence images of WT, HDAC10 KO, and HDAC10 KO cells treated with polyphyllin D (PPD; 1 μM). Cells were stained for lamin (green) and DNA (Hoechst; blue). White arrows indicate micronuclei, and boxed regions are enlarged in the adjacent panels. (Scale bar, 50 μm.) **g** Quantification of micronuclei relative to total nuclei in the groups shown in **f**. More than 100 nuclei were analyzed for each experiment. Data are presented as mean of 3 independent experiments with ± SD. **P < 0.01; ***P < 0.001, for the indicated comparisons.

Figure 6.

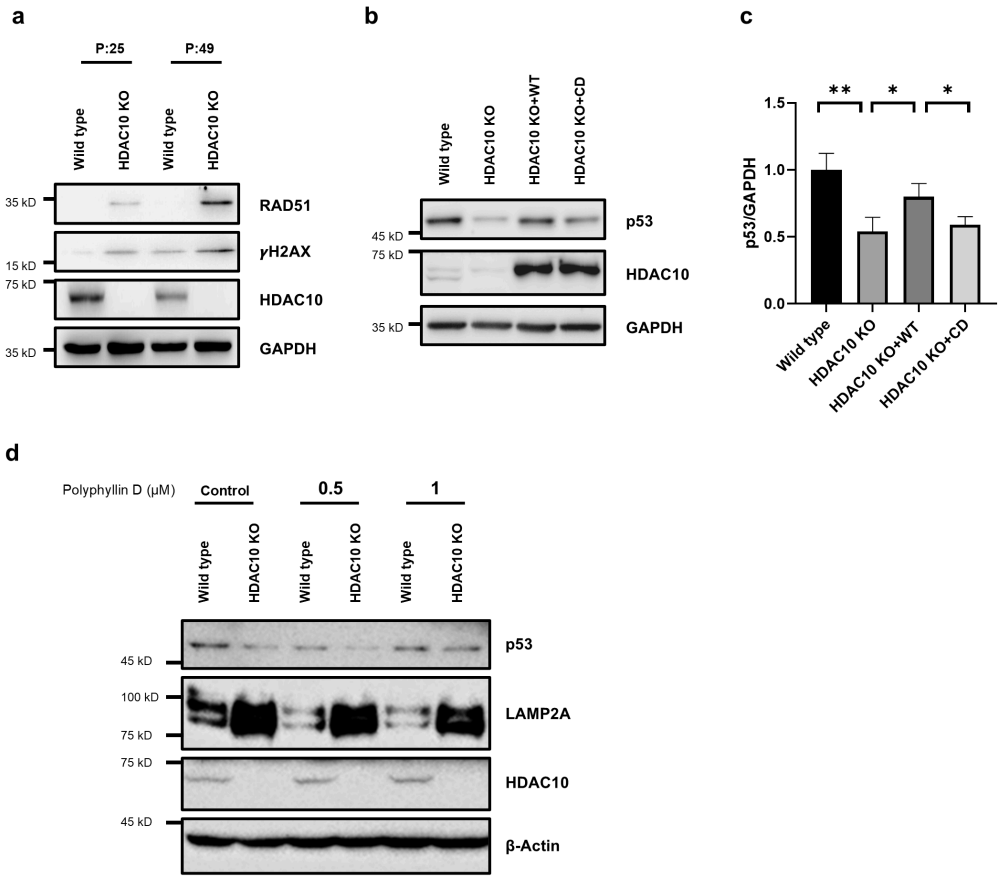

Figure 6

HDAC10 deficiency enhances DNA damage response but reduces p53 protein levels by CMA.

a Representative immunoblots of RAD51, γH2AX, and HDAC10 in WT and HDAC10 KO MEFs at passages 25 and 49. GAPDH served as the loading control. **b** Representative immunoblots of p53 and HDAC10 in WT, KO, KO+WT, and KO+CD MEFs. **c** Densitometric quantification of p53 normalized to GAPDH. Data are

presented as mean of 3 independent experiments ± SD. *$P < 0.05$; **$P < 0.01$, for the indicated comparisons. **d** Representative immunoblots of p53, LAMP2A, and HDAC10 in WT and KO MEFs treated with PPD (0.5 or 1 μM) or maintained under control conditions. β-Actin served as the loading control.

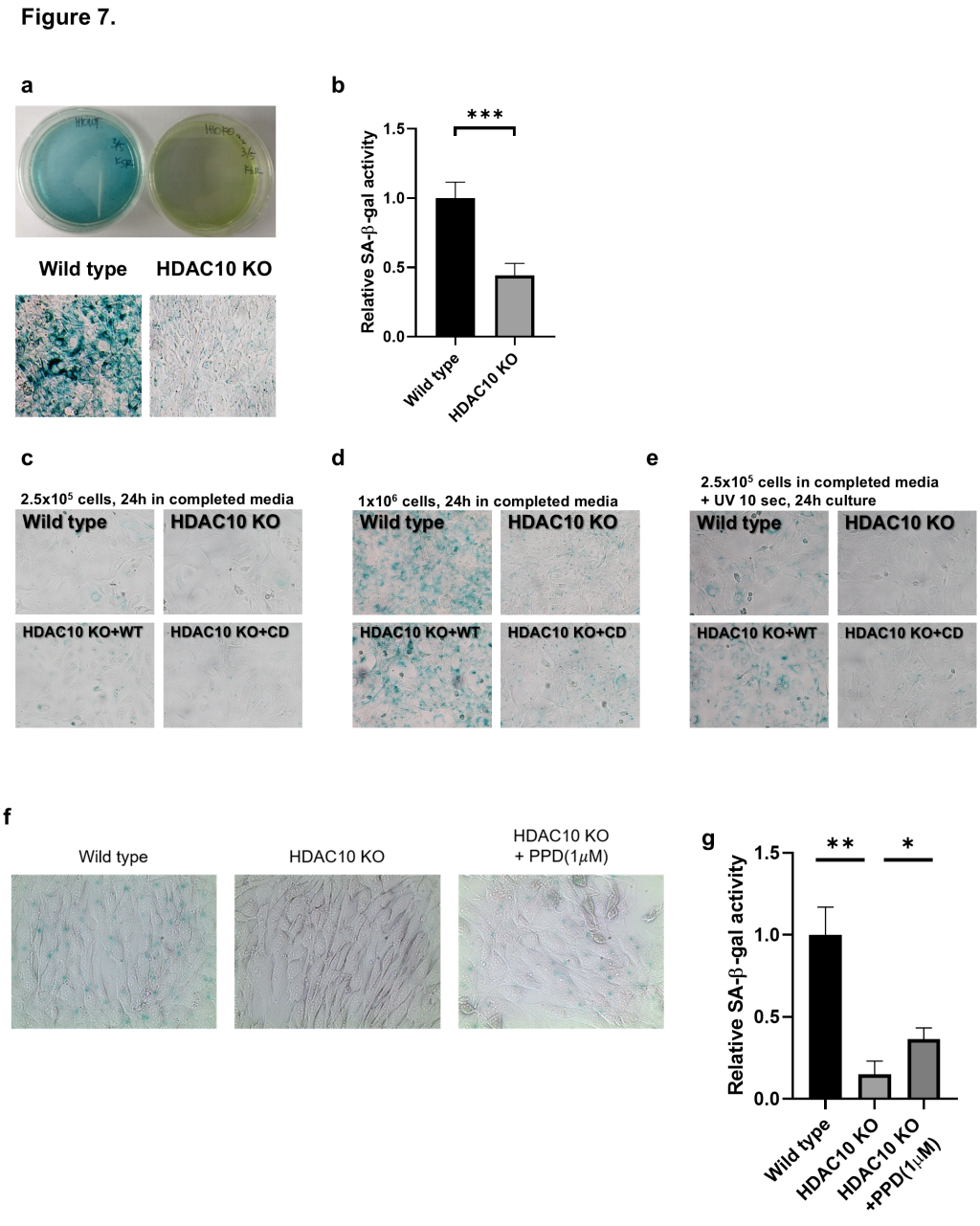

Figure 7

HDAC10 deficiency attenuates cellular senescence responses to high-density culture and UV exposure.

a Representative culture-dish photographs (top) and brightfield micrographs (bottom) showing senescence-associated β-galactosidase (SA-β-gal) staining in WT and HDAC10 KO MEFs after one week under contact-inhibition conditions. **b** Quantification of relative SA-β-gal activity for the conditions shown in **a**. Data are presented as mean ± SD. ***P* < 0.001. **c, d** Representative brightfield images of SA-β-gal staining in WT, KO, KO+WT, and KO+CD MEFs seeded at low density (2.5×10^5 cells; **c**) or high density (1×10^6 cells; **d**) and cultured in complete medium for 24 h. **e** Representative SA-β-gal staining in the same cell groups seeded at 2.5×10^5 cells, exposed to UV for 10 s, and cultured for a further 24 h. **f** Representative images of SA-β-gal staining in wild-type, HDAC10 KO, and HDAC10 KO cells treated with polyphyllin D (PPD; 1 μM). **g** Quantification of relative SA-β-gal activity. Data are presented as mean of 3 independent experiments with ± SD. **P* < 0.05; ***P* < 0.01, for the indicated comparisons.

Figure 8.

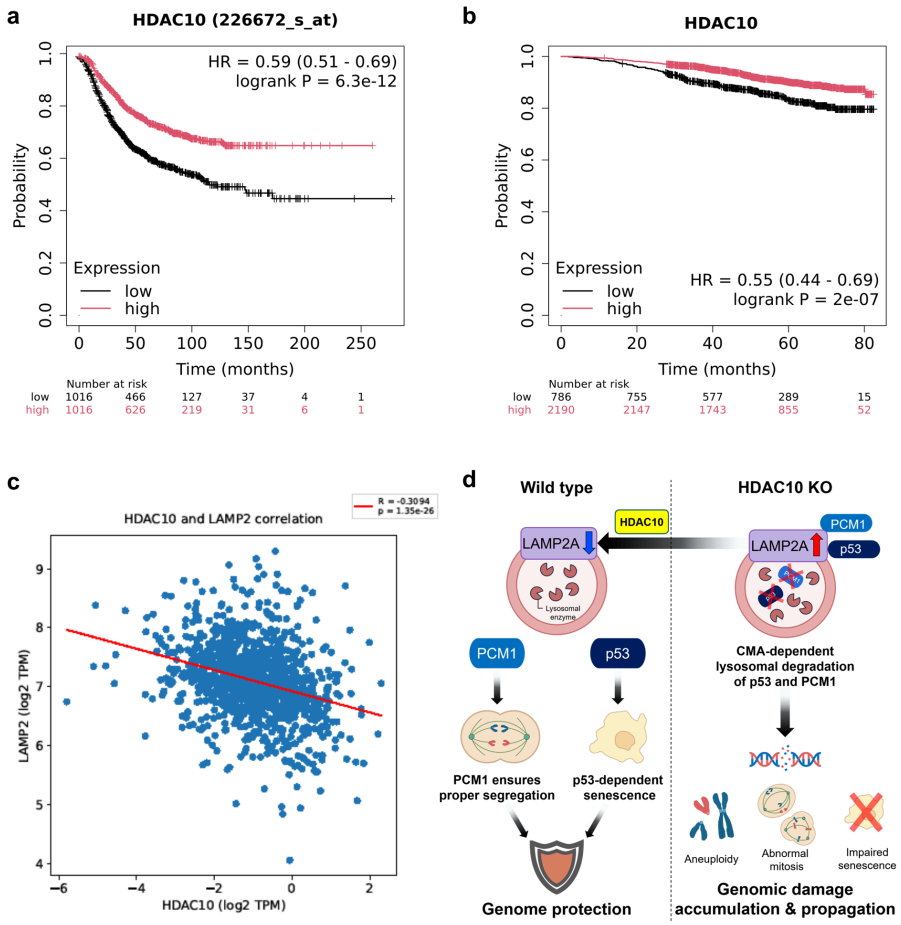

Figure 8

Association of HDAC10 expression with patient survival and LAMP2 expression in breast invasive carcinoma.

a, b Kaplan–Meier survival analyses of patients with breast cancer stratified by HDAC10 expression using microarray (**a**; probe 226672_s_at) and RNA-sequencing (**b**) datasets accessed through Kaplan–

Meier Plotter. Black and red curves represent low and high HDAC10 expression, respectively. Hazard ratios, 95% confidence intervals, log-rank *P* values, and numbers at risk are shown. **c** Correlation between HDAC10 and LAMP2 transcript levels in the breast invasive carcinoma (BRCA) dataset accessed through OncoDB. Expression is plotted as $\log_2$-transformed transcripts per million (TPM). The correlation coefficient and *P* value are indicated. **d** HDAC10 is proposed to limit excessive chaperone-mediated autophagy (CMA)-associated degradation of PCM1 and p53, thereby supporting faithful chromosome segregation and p53-dependent senescence, respectively. HDAC10 deficiency is associated with increased LAMP2A abundance and enhanced lysosomal degradation of PCM1 and p53, leading to mitotic abnormalities and impaired senescence. Together, these changes would promote the accumulation of genomic damage and the continued proliferation of genomically unstable cells.

Supplementary Files

This is a list of supplementary files associated with this preprint. Click to download.

- UGkimetalsuppl.docx
- SFig5.png
- SFig4.png
- SFig3.png
- SFig1.png
- SFig2.png
- Westernblotrawdata.docx